

Improving Geometry in Sparse-View 3DGS via Reprojection-based DoF Separation

Yongsung Kim^{1,*} Minjun Park^{1,*} Jooyoung Choi² Sungroh Yoon^{1,2,3,†}

¹Interdisciplinary Program in AI, Seoul National University

²ECE, ³AIIS, ASRI, INMC, ISRC, Seoul National University

{library753, minjunpark, jy_choi, sryoon}@snu.ac.kr

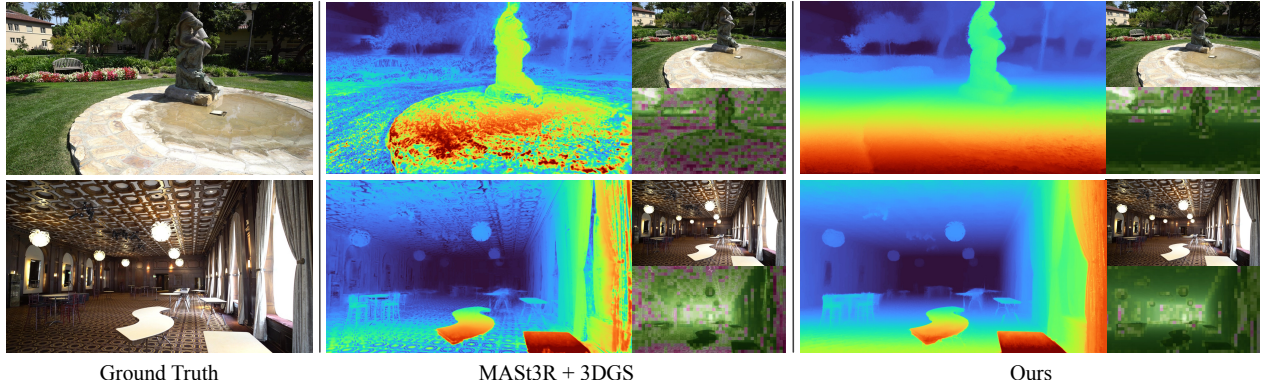


Figure 1. **3D reconstruction results with 12 views.** The image on the left side is the rendered depth image, and the upper right image is the rendered RGB image. The lower right image visualizes patch-wise depth correlation, where green indicates accurate geometry. As the color shifts from **green** to **gray** and then to **purple**, the patch-wise depth correlation decreases, indicating less plausible geometry. Our method qualitatively demonstrates more uniform and realistic geometry, which is also evident from the higher patch-wise depth correlation.

Abstract

Recent learning-based Multi-View Stereo models have demonstrated state-of-the-art performance in sparse-view 3D reconstruction. However, directly applying 3D Gaussian Splatting (3DGS) as a refinement step following these models presents challenges. We hypothesize that the excessive positional degrees of freedom (DoFs) in Gaussians induce geometry distortion, fitting color patterns at the cost of structural fidelity. To address this, we propose reprojection-based DoF separation, a method distinguishing positional DoFs in terms of uncertainty: image-plane-parallel DoFs and ray-aligned DoF. To independently manage each DoF, we introduce a reprojection process along with tailored constraints for each DoF. Through experiments across various datasets, we confirm that separating the positional DoFs of Gaussians and applying targeted constraints effectively suppresses geometric artifacts, producing reconstruction results that are both visually and geometrically plausible.

† Correspondence to: Sungroh Yoon (sryoon@snu.ac.kr)

* Both authors contributed equally to this work

1. Introduction

Advancements in augmented reality, autonomous driving, and robotics have heightened the demand for accurate 3D geometry reconstruction [1, 6]. While various depth sensors exist [32, 34], RGB camera-based reconstruction remains a cost-effective and scalable solution [22, 29, 37]. Traditional multi-view stereo (MVS) methods [15, 39] depend on robust feature-matching algorithms [3, 28] and require a large number of images to retain sufficient 3D features after outlier rejection [15, 37]. Although these approaches are successful, the need for many images limits their practicality in sparse-view scenarios [22, 29].

Deep learning has significantly advanced MVS capabilities, addressing the limitations of traditional methods. Seminal works DUS_t3R [49] and MAS_t3R [26] accurately estimate dense 3D geometry from multi-view images, making them ideal for initializing scenes for further refinement. Building upon these models allows us to focus on enhancing *geometric fidelity* rather than reconstructing scenes from scratch. However, directly refining the point clouds from MVS models using 3D Gaussian Splatting (3DGS) [22],

a differentiable rendering pipeline, can inadvertently degrade geometry, even when the initial point cloud is correctly structured. Figs. 1 and 2 illustrate geometric artifacts that arise during such refinement. We hypothesize that these artifacts originate from Gaussians overfitting during refinement by using their excessive positional degrees of freedom (DoFs) to fit texture, creating geometric inconsistencies.

To address the issues arising from excessive DoFs, we propose a novel approach that emphasizes the importance of separating DoFs based on their inherent uncertainties. By carefully distinguishing DoFs, we categorize them into two types: image-plane-parallel DoFs and ray-aligned DoF. This distinction is crucial, as each type has unique characteristics that affect stability during refinement. Image-plane-parallel DoFs, with lower uncertainty, are directly constrained by the observed pixels, whereas ray-aligned DoFs possess higher uncertainty and require multi-view information for accurate estimation. Recognizing these distinctions allows us to effectively limit unnecessary flexibility in the model, reducing the risk of overfitting.

To explicitly manage these separated DoFs, we introduce a *reprojection-based DoF separation* method that differentiates DoFs according to their respective uncertainties. In this method, we propose a *bounded offset* for image-plane-parallel DoFs, limiting their movement within a pixel. A secondary benefit of our method is that it preserves valuable per-view depth information from the MVS model, which would otherwise be lost in a naïve refinement approach. For the ray-aligned DoFs, we propose a *visibility loss* that leverages this depth information to refine the high-uncertainty DoFs through multi-view integration. By controlling each DoF with targeted constraints, our method achieves plausible geometric refinement—an aspect often overlooked in favor of rendered quality—while preserving rendering quality and minimizing geometric artifacts.

We evaluate our method on several novel view synthesis benchmarks, including Mip-NeRF 360 [2], which features complex camera trajectories; MVImgNet [58], characterized by object-centric scenes and simple camera trajectories; and Tanks and Temples [23], which includes unbounded scenes with simple camera trajectories. The effectiveness of our method is demonstrated through quantitative analysis, including PSNR and patch-wise Pearson correlation of depth maps, as well as qualitative visualizations.

Our contributions are as follows: (1) We introduce a reprojection-based DoF separation method that separates positional degrees of freedom (DoFs) by their uncertainties to address overfitting and geometric artifacts in MVS refinement. (2) We apply tailored constraints by limiting the movement of low-uncertainty DoFs within a pixel and refining high-uncertainty DoFs using per-view depth information. (3) Our approach consistently improves geometry without compromising rendering quality, as evidenced

by comprehensive quantitative and qualitative evaluations across diverse benchmarks [2, 23, 58].

2. Related Work

2.1. Multi-View-Stereo

Multi-View-Stereo (MVS) aims to generate dense 3D geometry from calibrated images. Traditional MVS methods rely on camera parameters from Structure from Motion (SfM) [38, 41] or Simultaneous Localization and Mapping (SLAM) [11, 30] and are categorized by their geometric representations: volumetric, point-cloud, or depth map-based approaches. Volumetric methods use voxels but incur high memory costs [13, 24, 40, 59]. Point cloud-based methods [14–16, 38] densify sparse point clouds from SfM. Depth map-based methods [17, 38, 55, 61] estimate per-view depth maps and fuse them for 3D reconstruction. However, traditional MVS struggles with surfaces that have complex illumination or lack texture due to reliance on hand-crafted feature-matching algorithms [3, 28].

Learning-based MVS methods [47] address these challenges by leveraging neural networks. Among the various approaches, some use voxels to represent the scene [8, 21, 31, 43], while others rely on depth maps to reconstruct the 3D structure [7, 18, 46, 48, 56]. NeRF [29] and 3D Gaussian Splatting (3DGS) [22] are applied to perform MVS, but they require a large number of images and substantial computational resources.

The latest advancements are large-scale MVS models such as DUST3R [49], MAST3R [26] and PixelSplat [5]. These transformer-based models, trained on extensive datasets, perform end-to-end MVS tasks efficiently, even in sparse-view conditions, handling camera calibration, relative pose estimation, and dense point cloud reconstruction.

2.2. Sparse-View 3D Reconstruction

3D reconstruction typically requires a large number of images [22, 29]. While neural radiance fields [2, 29, 35] can generate high-quality renderings from images alone, they generally need hundreds of images to learn a scene. To improve efficiency, various methods [9, 19, 20, 25, 27, 33, 51–53, 62] have emerged to learn 3D scenes from only a few views.

There are two main approaches for 3D reconstruction with sparse views. The first approach relies solely on the available sparse-view data, using techniques such as depth smoothness constraints [33] or masked positional encoding and occlusion regularization [53] to prevent overfitting and suppress artifacts. However, as the number of views decreases, this data-only approach may not achieve sufficient quality. To overcome this limitation, the second approach incorporates external knowledge, such as color information through normalizing flow models [33] or feature ex-

tractors to maintain visual and semantic consistency across rendered views [20, 25] or personalized diffusion models [52]. Because most NeRF and 3DGS rely on color-based losses, they can suffer from overfitting on texture, leading to a degradation in geometry quality when the number of training views is limited [53, 62]. Some studies leverage the depth of prior knowledge from pretrained models. For instance, depth maps generated by monocular depth estimators can act as valuable geometry priors [9, 19, 27, 51, 62].

2.3. Sparse-View 3DGS with Learning-based MVS

Unlike traditional approaches that train 3DGS initialized with sparse point clouds from SfM, [12, 52] initialize Gaussians with dense point clouds from learning-based MVS, achieving high novel-view synthesis performance even with few images. However, during training, the geometry produced by learning-based MVS models often degrades.

3. Preliminary

Learning-based MVS Methods including DUS_t3R [49] and MAS_t3R [26] are learning-based multi-view stereo (MVS) methods designed to perceive 3D geometry from unconstrained multi-view images. Leveraging prior knowledge from large-scale training, they successfully reconstruct dense 3D point clouds even in sparse-view conditions, where traditional MVS methods often struggle. Building upon the architecture of DUS_t3R, MAS_t3R incorporates an additional head for correspondence matching, enhancing its performance in estimating camera calibration, relative poses, and dense point cloud reconstruction in a single forward pass. These models leverage a transformer-based encoder-decoder architecture [10, 45], utilizing cross-attention in the decoder to capture inter-view information by processing pairs of images.

To handle multi-view geometry, DUS_t3R and MAS_t3R simplify the problem by breaking it down into sets of two-view geometries. They then employ a global alignment strategy to merge pairwise predictions into a shared coordinate system. To lighten the optimization, multi-view geometry consistency is disregarded during global alignment. While this approach is efficient and well-suited to deep

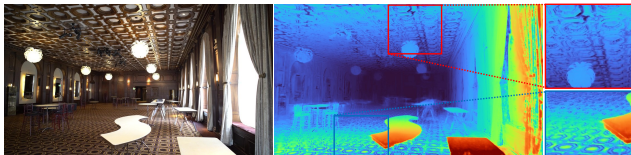


Figure 2. **Geometric artifacts from naive 3DGS refinement.** Texture representation via Gaussian positions introduces unintended geometric patterns. The red box highlights excessive distortion in the ceiling geometry, and the blue box shows gaps in the flat floor geometry following texture patterns.

learning frameworks, it can lead to suboptimal geometry because the optimization process disregards information from other views, leading to a lack of geometric consistency. It makes further refinement necessary.

3D Gaussian Splatting (3DGS) is a recent differentiable rendering technique that represents scenes using 3D Gaussians as primitives. It initializes the scene with a sparse point cloud, typically obtained from Structure-from-Motion (SfM) [37] and assigns these points as the means of the Gaussians. The differentiable rasterizer in 3DGS allows for scene refinement using photometric loss, making it compatible with incorporation after an MVS module like MAS_t3R.

However, directly refining the point cloud from MAS_t3R using 3DGS can introduce geometric artifacts, such as floaters and unintended geometric patterns aligned with textures, as shown in Fig. 2. These issues highlight the need for a more careful integration and refinement strategy to preserve the geometric fidelity of the reconstruction.

4. Method

We aim to reconstruct a visually and geometrically plausible scene from a limited set of images. In Sec. 4.1, we initialize the scene using a learning-based multi-view stereo (MVS) model. Next, Sec. 4.2 differentiates the Degrees of Freedom (DoFs) and proposes a reprojection-based DoF separation method that highlights their uncertainty difference. Finally, in Sec. 4.3, we formulate constraints for each DoF type, reducing unnecessary DoFs and enabling geometrically stable refinement even in sparse-view scenarios.

4.1. MVS Initialization

We use MAS_t3R [26], a variant of DUS_t3R [49], to initialize the scene. Compared to DUS_t3R, MAS_t3R includes an additional head for correspondence matching, offering improved performance. While MAS_t3R provides added functionality, its role in our context remains the same: it takes images as input and outputs a dense point cloud along with estimated camera poses. A formal description of MAS_t3R’s behavior is as follows:

$$\text{MAS}_{t3R} : \{I_i\}_{i=1}^N \rightarrow \{(D_i, T_i)\}_{i=1}^N \rightarrow \{X_i\}_{i=1}^N, \quad (1)$$

where I_i is the input image from view i ; D_i represents the predicted per-view depth map for I_i ; T_i denotes the transformation from pixel coordinates to world coordinates, parameterized by the camera pose and intrinsic parameters; and X_i represents the unprojected 3D points for view i , computed using the D_i and T_i .

The top row of Fig. 3 shows a schematic of the behavior common to learning-based MVS models like DUS_t3R and MAS_t3R, along with a naïve approach that treats MAS_t3R as a black-box initializer. This setup feeds the MVS point cloud into 3DGS for scene refinement.

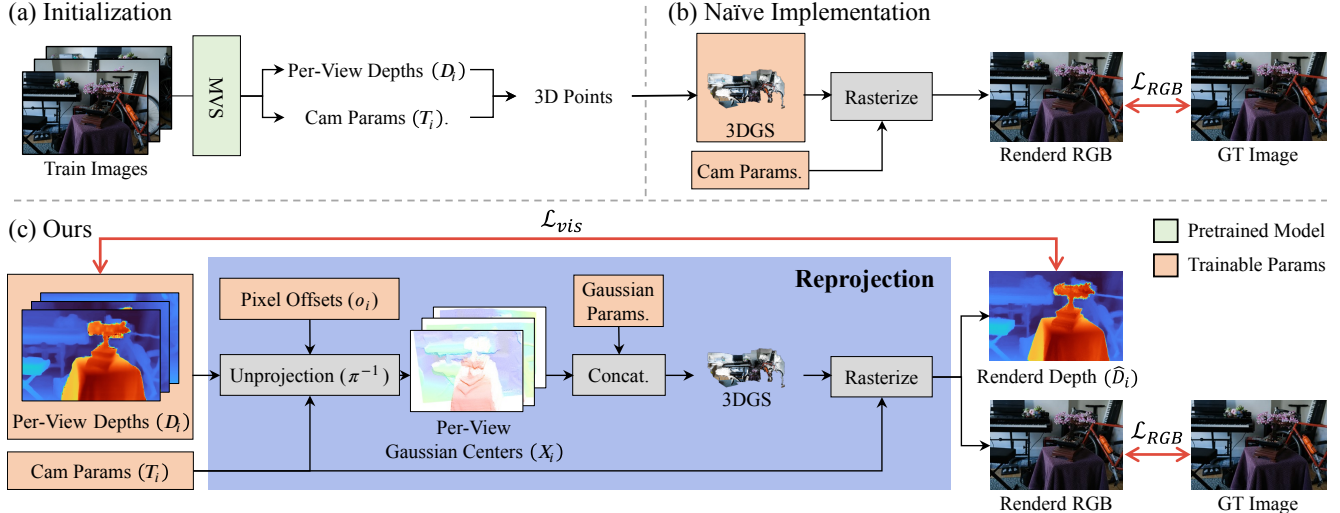


Figure 3. **Overview of the proposed framework.** (a) Scene initialization using a learning-based MVS model, which predicts 3D points from images and outputs per-view depth as an intermediate representation. (b) Naïve implementation, where MVS is treated as a black-box model, and its output is refined using the 3DGS pipeline. (c) Our proposed framework, which introduces reprojection-based refinement by retaining intermediate per-view depth as a trainable target. A visibility loss function is used to resolve conflicts when aligning individual per-view depths into a shared coordinate system.

4.2. Reprojection-based DoF Separation

Refining the output of the MVS with 3DGS introduces geometric artifacts along texture as shown in Fig. 2. We hypothesize that this is because Gaussians leverage their excessive positional DoFs to reduce photometric loss, resulting in geometric artifacts due to overfitting. To address this, we differentiate the positional DoFs to limit the model’s excessive flexibility while retaining sufficient DoFs for accurate geometric refinement.

We propose to separate each Gaussian’s three positional DoFs into two distinct components: (1) *image-plane-parallel DoFs* that are parallel to the image plane and (2) a *ray-aligned DoF* along the pixel ray direction. Our key insight is that these DoFs exhibit different levels of uncertainty. Image-plane-parallel DoFs are directly observed in the image and thus have low uncertainty, bounded by the pixel size. In contrast, the ray-aligned DoF remains inherently ambiguous from a single view and requires multi-view information for refinement. This separation is illustrated in the left column of Fig. 4, where the possible positions of an unprojected point form a viable frustum along the pixel ray.

To make an explicit distinction during refinement, we introduce a *reprojection-based DoF separation* method. This method retains per-view depth, an intermediate representation of the learning-based MVS model, and unprojects pixels to retrieve 3D Gaussians for each render. We then attach Gaussian parameters to these points for integration with the 3DGS pipeline [22]. This allows us to use the 3DGS rasterizer to reproject the Gaussians onto the image plane, effectively rendering views. The ray-aligned DoF corresponds

to the per-view depth in this context. Image-plane-parallel DoFs are implemented by allowing small offsets o_i from the pixel center when calculating a pixel ray for the unprojection. The overall pipeline of this method is highlighted by the blue box in Fig. 3.

Reprojection-based DoF separation provides granular control over two distinct types of DoFs. Additionally, it retains per-view depth estimations D_i from the MVS model, which would otherwise be lost in a naïve approach. The global alignment in the MVS model removes shift-scale ambiguity [36] present in methods that use a monocular depth estimator for each view [42, 44]. This ambiguity-free depth information serves as a valuable prior for robust refinement. In Sec. 4.3, we describe how this depth information is incorporated into our refinement framework, maximizing the potential of the learning-based MVS model beyond simple initialization.

4.3. Bounded Offset & Visibility Loss

To refine geometry while avoiding artifacts, we propose specific constraints for each type of DoF in our model. We elaborate on two essential conditions to ensure reprojection faithfully recovers the original views. First, the unprojected 3D point must remain within the frustum formed by rays passing through the four corners of its corresponding pixel; otherwise, it may project onto a neighboring pixel. Additionally, the point should avoid being occluded by other Gaussians in the scene, which can occur when integrating multiple views within a global coordinate system. These conditions are illustrated by the failure cases in Fig. 4.

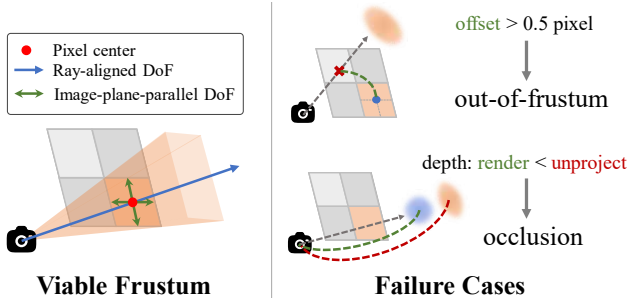


Figure 4. **Separation of DoFs.** The left column illustrates the two types of positional degrees of freedom (DoFs): ray-aligned and image-plane-parallel. The right column shows two scenarios where a point fails to project back to its original pixel.

Bounded Offset. For the first condition, we control image-plane-parallel DoFs by limiting the offset applied to the pixel coordinates during unprojection. Specifically, we add an offset within ± 0.5 pixel units before transforming pixel coordinates into world coordinates. This ensures the 3D point stays within the viable frustum and projects back onto its original pixel. Deviating from this constraint causes the point to project incorrectly, as shown in the *out-of-frustum* example in Fig. 4. The unprojection with bounded offset is formally expressed as:

$$\delta_i = 0.5 \cdot \tanh(o_i), \quad (2)$$

$$X_i = \pi^{-1}(p + \delta_i, D_i) \cdot T_i, \quad (3)$$

where p represents the pixel center coordinates, o_i denotes the learned 2D offset, $\pi^{-1} : \mathbb{R}^2 \times \mathbb{R} \rightarrow \mathbb{R}^3$ is the inverse projection function, D_i is the depth map, and T_i represents the camera transformation matrix. The value 0.5 in Eq. (2) represents the maximum offset. This step corresponds to the early stage of the projection process in Fig. 3, where pixel offsets are input to the unprojection function π^{-1} .

Visibility Loss. For the second condition, we address occlusion by defining a visibility loss. Occlusions are detected by comparing the per-view estimated depth (representing the ray-aligned DoF) with the rendered depth (which incorporates multi-view information). If the rendered depth is smaller than the per-view depth, it indicates that another Gaussian obstructs the ray, as illustrated in the *occlusion* scenario of Fig. 4. The visibility loss is defined as the L2 distance between these two depths, encouraging the unprojected point to remain visible and resolving geometry conflicts introduced by multi-view alignment. Formally, the visibility loss \mathcal{L}_{vis} is expressed as:

$$\mathcal{L}_{vis} = \|\hat{D}_i - D_i\|_2^2, \quad (4)$$

where \hat{D}_i and D_i denote the rendered depth and per-view depth estimated by MVS from view i , respectively.

5. Experiment

5.1. Experimental Setup

Datasets. We evaluate our method on Tanks and Temples [23], Mip-NeRF 360 [2], and MVImgNet [58]. Mip-NeRF 360 features complex camera trajectories, MVImgNet includes object-centric scenes, and Tanks and Temples consists of unbounded forward-facing scenes. We use eight scenes from Tanks and Temples and seven from MVImgNet to align with baseline methods [12, 22].

Metrics. We assess 3D reconstruction quality using PSNR, SSIM [50], and LPIPS [60] for image fidelity. For geometry plausibility, we compare rendered depth maps with those from a monocular depth estimator [54] using Pearson correlation to address scale ambiguity. Additionally, inspired by DNGaussian [27], we compute patch-wise depth Pearson correlation (PDC) to capture local geometric details and use the average of all patches to evaluate the overall geometry of the image. To visualize PDC, we overlay it in color on the corresponding patches of the depth map: green indicates high PDC values and plausible geometry, gray represents intermediate values, and purple signifies low PDC values, indicating implausible geometry.

Baselines. We use a naïve implementation as baseline, where we train 3DGS, initialized with the point cloud generated by MAST3R. Additionally, we compare with InstantSplat [12], demonstrating state-of-the-art performance among methods using learning-based MVS. It enhances both the efficiency and reconstruction quality of the naïve approach by applying grid-based, confidence-aware Farthest Point Sampling.

Implementation Details. We implement our method using the gsplat [57] library and trained for 10,000 iterations. We render at a resolution of 512 for the first 2,000 iterations and at the input image resolutions for the remaining 8,000. After 2,000 iterations, rendered depth maps are downsampled to match per-view resolutions for loss computation. Spherical harmonics degrees increase from 0 to 3 every 100 iterations. To prevent Gaussians from scaling excessively, we project them onto image planes and apply scale clipping at 30 pixels, following MAST3R’s configuration. For the visibility loss, we apply a linear scheduling strategy, gradually decreasing it over 10,000 iterations.

Aligning Test Views on Geometry. Unlike conventional methods that require highly accurate poses obtained from COLMAP [37] using hundreds of images, our approach performs reconstruction using camera poses derived from a learning-based MVS with up to 12 images. Following NopeNeRF [4] and InstantSplat [12], we perform 500 iterations of optimization for each test view, learning only the camera extrinsic parameters while keeping the scene frozen.

Method	Mip-NeRF 360 [2]				MVImgNet [58]			
	PSNR \uparrow	SSIM \uparrow	LPIPS \downarrow	PDC \uparrow	PSNR \uparrow	SSIM \uparrow	LPIPS \downarrow	PDC \uparrow
InstantSplat [12]	17.84	0.4468	0.4359	0.1248	23.23	<u>0.7313</u>	0.2707	0.1133
InstantSplat \dagger [12]	17.47	0.4163	0.4156	0.1528	23.51	0.7517	0.2182	0.1320
MASt3R [26]+3DGS [22]	<u>18.84</u>	0.4786	<u>0.4089</u>	<u>0.1537</u>	<u>23.53</u>	0.7154	0.2555	<u>0.3474</u>
Ours	19.38	<u>0.4767</u>	0.3716	0.3958	23.57	0.7232	<u>0.2290</u>	0.4130

Table 1. **Quantitative comparison on Mip-NeRF 360 and MVImgNet.** All scenes are trained with 12 views. PDC denotes patch-wise depth Pearson correlation. The best results are highlighted in bold, and the second-best results are underlined. InstantSplat indicated with \dagger refers to the model trained for 10,000 iterations. Our method demonstrates higher patch-wise Pearson correlation values.

Method	PSNR \uparrow	SSIM \uparrow	LPIPS \downarrow	PDC \uparrow
InstantSplat	22.22	<u>0.7495</u>	0.1966	<u>0.3006</u>
InstantSplat \dagger	21.99	0.7276	<u>0.1897</u>	0.2446
MASt3R+3DGS	<u>22.42</u>	0.7451	0.2088	0.2452
Ours	22.80	0.7501	0.1848	0.6019

Table 2. **Quantitative comparison on Tanks and Temples.** All scenes are trained using 3 views. InstantSplat indicated with \dagger refers to the model trained for 10,000 iterations. Our method achieves high performance not only in geometry reconstruction but also in novel-view synthesis.

5.2. Comparisons

Quantitative results. Tab. 1 shows the quantitative results for training on 12 views from the Mip-NeRF 360 and MVImgNet datasets. The Mip-NeRF 360 dataset, with its complex camera trajectories, allows test views to reveal geometric distortions thoroughly. In such challenging scenes, our method improves the plausibility of geometry reconstruction, resulting in a significant PSNR increase. MVImgNet and Tanks and Temples have simpler camera parameters compared to Mip-NeRF 360. This allows the baselines to perform novel view synthesis through simple interpolation between views [4]. However, they fail to reconstruct plausible geometry due to overfitting to texture, which is reflected in lower PDC scores. In contrast, our method demonstrates comparable novel view synthesis performance while simultaneously reconstructing plausible geometry as shown in Tabs. 1 and 2. Additionally, Tab. 2 presents results for training on only three images from Tanks and Temples, demonstrating that our method reconstructs geometry with high fidelity, even in scenarios with very limited training images.

Qualitative results. Figs. 5 to 7 present the visual comparison results. The qualitative results show that the baselines and our method perform comparably in novel view synthesis. However, there is a clear difference in the quality of the rendered depth maps. The baselines tend to distort geometry to represent texture. For example, as illus-

trated in Fig. 5, in the Francis scene from the Tanks and Temples dataset, the ground geometry is distorted to create gaps that mimic the grid pattern in the floor texture. The bottom row of each scene visualizes the PDC. PDC values are represented with a color scale: patches closer to 1 are shown in green, 0 in gray, and -1 in red. Our method demonstrates high PDC values not only for objects in object-centric scenes but also for surfaces like floors and ceilings. This indicates that our method achieves a more plausible geometry reconstruction.

5.3. Ablation Study

Bounded Offset. In Tabs. 1 and 2, comparisons with 3DGS initialized by MASt3R demonstrate that learning the positional DoF of Gaussians with a bounded offset enables plausible geometry reconstruction. Therefore, we conduct an ablation study on learning the offset. To evaluate the effect of learning the offset, we fix the maximum offset to zero and train on the Tanks and Temples dataset using 12 views. As shown in Tab. 3, when the offset is not learned, there is a marginal change in the PDC, indicating little impact on the learned geometry. However, omitting offset training consistently degrades novel-view synthesis performance, as PSNR measures. Conversely, in the case of 3D Gaussian Splatting initialized naively with MASt3R, both PSNR and PDC exhibit low values. Therefore, we observe that the bounded offset contributes to the reconstruction quality in terms of both geometry and rendering quality.

Visibility Loss. We investigate the impact of visibility loss by comparing results from training on the Tanks and Temples dataset with and without its application. Tab. 3 shows that omitting the visibility loss degrades PDC performance across all scenes, confirming that this loss contributes to learning more accurate geometry. Improved geometry, as reflected in higher PDC, also enhances rendering quality, as evidenced by the slight drop in PSNR when the visibility loss is omitted. This contribution is not only reflected in the PDC values but also visually in the suppression of geometrical artifacts, as shown in Fig. 8.

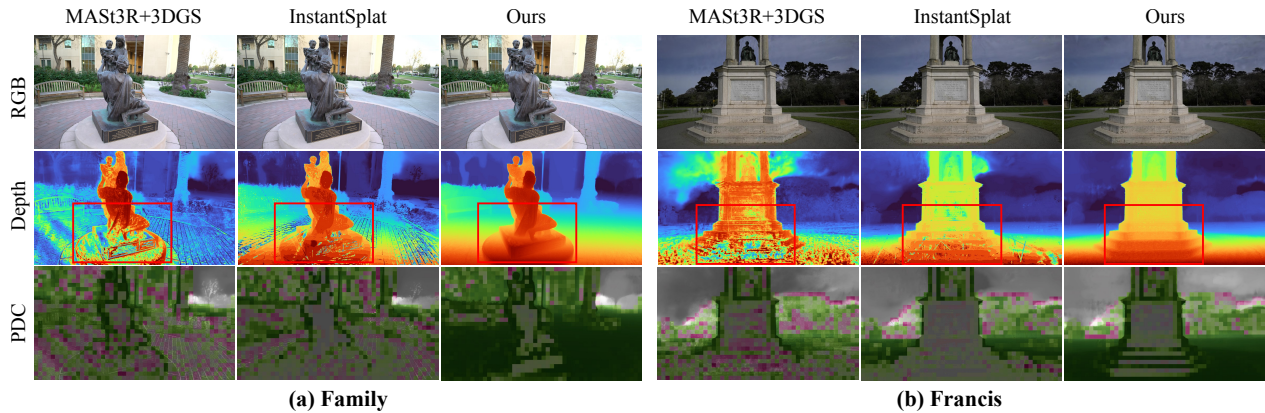


Figure 5. **Qualitative comparison on Tanks and Temples.** Our method outperforms the baselines not only in reconstructing smooth surfaces, such as the floor, but also in capturing the geometry of complex shapes like statues. As the color shifts from **green** to **gray** and then to **purple**, the patch-wise depth correlation decreases, indicating less plausible geometry.

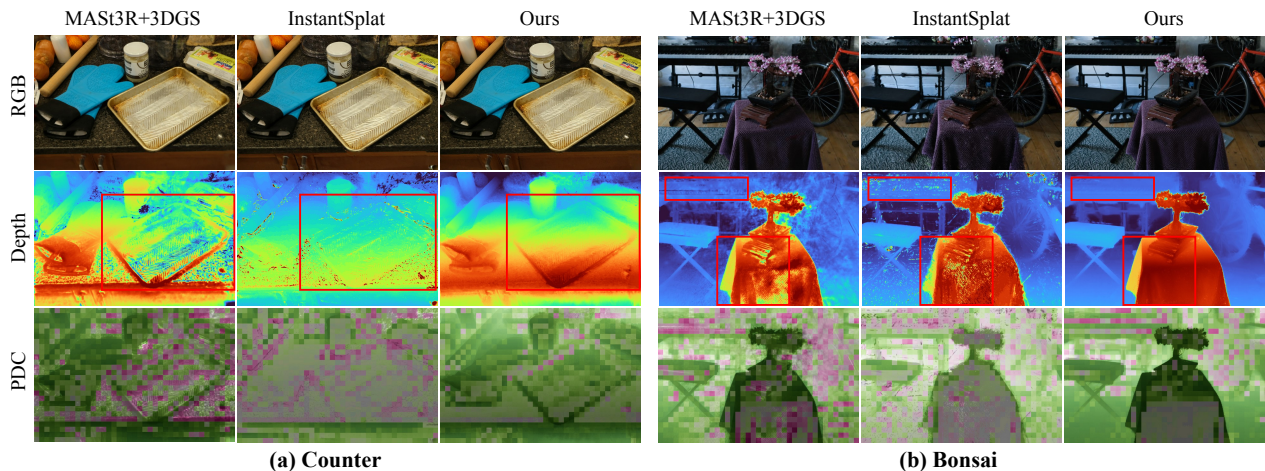


Figure 6. **Qualitative comparison on Mip-NeRF 360.** In the Counter scene, the baselines represent the patterns of the tray and tablecloth as geometric artifacts, whereas our method more plausibly captures the geometry. Additionally, in the Bonsai scene, the baselines produce numerous floaters near the piano and bicycle, while our method represents the geometry without floaters.

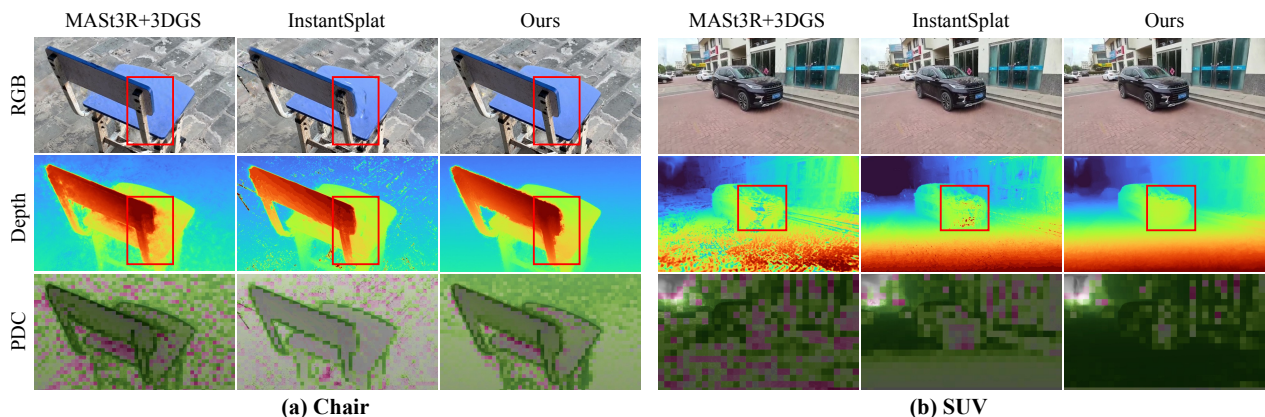


Figure 7. **Qualitative comparison on MVImgNet.** The baselines distort the geometry to represent the texture of the surface of the chair and ground, resulting in geometric artifacts that are identifiable not only in the depth map but also in the RGB image. In the SUV scene, our method generates a convex geometry on the front of the SUV, whereas the baselines produce a distorted geometry.

	3-shots						12-shots					
	Ours		w/o Offset		w/o \mathcal{L}_{vis}		Ours		w/o Offset		w/o \mathcal{L}_{vis}	
	PSNR \uparrow	PDC \uparrow	PSNR \uparrow	PDC \uparrow	PSNR \uparrow	PDC \uparrow	PSNR \uparrow	PDC \uparrow	PSNR \uparrow	PDC \uparrow	PSNR \uparrow	PDC \uparrow
Ballroom	24.01	0.7766	23.95	0.7743	24.28	0.7551	30.56	0.8114	30.05	0.8093	30.64	0.7874
Barn	21.90	0.5413	21.78	0.5391	21.31	0.5029	28.33	0.5931	28.12	0.5924	27.89	0.5343
Church	19.19	0.7033	19.07	0.7022	18.74	0.6890	23.55	0.7597	23.51	0.7622	23.42	0.7155
Family	24.11	0.6552	24.01	0.6522	23.47	0.5714	29.49	0.6870	29.20	0.6873	29.42	0.6076
Francis	23.99	0.3739	23.73	0.3655	23.54	0.3356	31.43	0.4022	30.49	0.4007	31.23	0.3679
Horse	23.25	0.4373	23.23	0.4384	23.15	0.3857	28.49	0.4602	28.23	0.4592	28.21	0.4034
Ignatius	23.36	0.7163	22.52	0.7108	23.32	0.6684	27.81	0.7525	26.28	0.7444	27.73	0.7038
Museum	22.61	0.6115	22.41	0.5928	22.52	0.5616	28.63	0.6729	28.59	0.6704	28.52	0.6046
Avg.	22.80	0.6019	22.59	0.5969	22.54	0.5587	28.54	0.6424	28.06	0.6407	28.38	0.5906

Table 3. **Impact of bounded offset and visibility loss.** PDC denotes patch-wise Pearson correlation. The best results are highlighted in bold. Results with 3-shot training, extremely sparse-view condition, are shown on the left, and 12-shot training on the right.

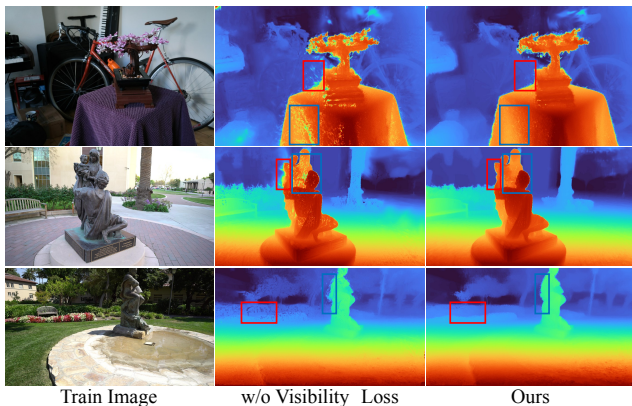


Figure 8. **Results of the visibility loss ablation study.** Each row presents the RGB image of a training view, the depth image without the visibility loss, and the depth image from our complete method. Omitting the visibility loss increases floaters and bumpy surfaces along textures.

6. Limitation and Future Work

We analyze cases where our method fails to reconstruct geometry plausibly and identify two major failure types inherited from MAST3R. First, MAST3R’s error in camera pose estimation causes misalignment among unprojected per-view geometries, resulting in overlapped geometries, as shown in Fig. 9. Second, we observe that MAST3R interprets specular surfaces as excessively hollow, causing them to remain hollow even after refinement. These issues could potentially cause common problems not only in our method but in all approaches that use learning-based MVS. Therefore, future research directions could include more accurate camera pose estimation for global alignment in learning-based MVS or developing methods for accurately understanding the geometry of specular surfaces.

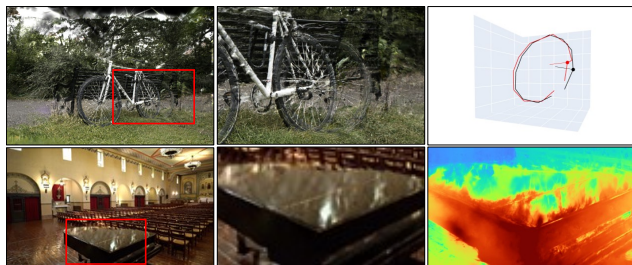


Figure 9. **Limitations inherited from the MAST3R.** The first row illustrates failures from MAST3R’s inaccurate camera pose estimation, resulting in the bicycle wheel’s overlapping geometries. The second row presents failures caused by specular surfaces, where the geometry of the piano is distorted in the reconstruction, with flat surfaces appearing hollow.

7. Conclusion

In this work, we proposed the *reprojection-based DoF separation* to improve geometry quality in sparse-view reconstruction, starting from dense geometry obtained with a learning-based MVS model. We showed that photometric refinement without addressing excessive degrees of freedom (DoFs) leads to geometry degradation. To address this, we separated the positional DoFs of Gaussians into image-plane-parallel and ray-aligned components based on their levels of uncertainty. To explicitly manage each DoF, we proposed a reprojection-based DoF separation method. Additionally, we introduced targeted constraints for DoF, considering their uncertainties, specifically bounded offset and visibility loss. We showed that our method consistently enhances geometry quality across various dataset types. Through this study, we showed that geometry quality is not fully captured by PSNR, and we hope that future research utilizing learning-based MVS will move beyond PSNR to also consider geometric plausibility.

8. Acknowledgements

This work was supported by Samsung Electronics Co., Institute of Information & communications Technology Planning & Evaluation (IITP) grant funded by the Korea government(MSIT) [NO.RS-2021-II211343, Artificial Intelligence Graduate School Program (Seoul National University)], the National Research Foundation of Korea (NRF) grant funded by the Korea government (MSIT) (No. 2022R1A3B1077720, 2022R1A5A708390811), and the BK21 Four program of the Education and Research Program for Future ICT Pioneers, SNU in 2024.

References

- [1] William Agnew, Christopher Xie, Aaron Walsman, Octavian Murad, Yubo Wang, Pedro Domingos, and Siddhartha Srinivasa. Amodal 3d reconstruction for robotic manipulation via stability and connectivity. In *Conference on Robot Learning*, pages 1498–1508. PMLR, 2021. 1
- [2] Jonathan T. Barron, Ben Mildenhall, Dor Verbin, Pratul P. Srinivasan, and Peter Hedman. Mip-nerf 360: Unbounded anti-aliased neural radiance fields. *CVPR*, 2022. 2, 5, 6
- [3] Herbert Bay. Surf: Speeded up robust features. *Computer Vision—ECCV*, 2006. 1, 2
- [4] Wenjing Bian, Zirui Wang, Kejie Li, Jiawang Bian, and Victor Adrian Prisacariu. Nope-nerf: Optimising neural radiance field with no pose prior. In *CVPR*, 2023. 5, 6
- [5] David Charatan, Sizhe Li, Andrea Tagliasacchi, and Vincent Sitzmann. pixelsplat: 3d gaussian splats from image pairs for scalable generalizable 3d reconstruction. In *CVPR*, 2024. 2
- [6] Siheng Chen, Baoan Liu, Chen Feng, Carlos Vallespi-Gonzalez, and Carl Wellington. 3d point cloud processing and learning for autonomous driving: Impacting map creation, localization, and perception. *IEEE Signal Processing Magazine*, 38(1):68–86, 2021. 1
- [7] Shuo Cheng, Zexiang Xu, Shilin Zhu, Zhuwen Li, Li Erran Li, Ravi Ramamoorthi, and Hao Su. Deep stereo using adaptive thin volume representation with uncertainty awareness. In *Proceedings of the IEEE/CVF conference on computer vision and pattern recognition*, pages 2524–2534, 2020. 2
- [8] Christopher B Choy, Danfei Xu, JunYoung Gwak, Kevin Chen, and Silvio Savarese. 3d-r2n2: A unified approach for single and multi-view 3d object reconstruction. In *Computer Vision—ECCV 2016: 14th European Conference, Amsterdam, The Netherlands, October 11-14, 2016, Proceedings, Part VIII 14*, pages 628–644. Springer, 2016. 2
- [9] Kangle Deng, Andrew Liu, Jun-Yan Zhu, and Deva Ramanan. Depth-supervised nerf: Fewer views and faster training for free. In *Proceedings of the IEEE/CVF Conference on Computer Vision and Pattern Recognition*, pages 12882–12891, 2022. 2, 3
- [10] Alexey Dosovitskiy, Lucas Beyer, Alexander Kolesnikov, Dirk Weissenborn, Xiaohua Zhai, Thomas Unterthiner, Mostafa Dehghani, Matthias Minderer, Georg Heigold, Sylvain Gelly, Jakob Uszkoreit, and Neil Houlsby. An image is worth 16x16 words: Transformers for image recognition at scale. *ICLR*, 2021. 3
- [11] Jakob Engel, Thomas Schöps, and Daniel Cremers. Lsdslam: Large-scale direct monocular slam. In *European conference on computer vision*, pages 834–849. Springer, 2014. 2
- [12] Zhiwen Fan, Wenyan Cong, Kairun Wen, Kevin Wang, Jian Zhang, Xinghao Ding, Danfei Xu, Boris Ivanovic, Marco Pavone, Georgios Pavlakos, Zhangyang Wang, and Yue Wang. Instantsplat: Unbounded sparse-view pose-free gaussian splatting in 40 seconds, 2024. 3, 5, 6
- [13] J-S Franco and Edmond Boyer. Fusion of multiview silhouette cues using a space occupancy grid. In *Tenth IEEE International Conference on Computer Vision (ICCV’05) Volume 1*, pages 1747–1753. IEEE, 2005. 2
- [14] Simon Fuhrmann, Fabian Langguth, and Michael Goesele. Mve-a multi-view reconstruction environment. *GCH*, 3:4, 2014. 2
- [15] Yasutaka Furukawa and Jean Ponce. Accurate, dense, and robust multiview stereopsis. *IEEE transactions on pattern analysis and machine intelligence*, 32(8):1362–1376, 2009. 1
- [16] Yasutaka Furukawa, Brian Curless, Steven M Seitz, and Richard Szeliski. Towards internet-scale multi-view stereo. In *2010 IEEE computer society conference on computer vision and pattern recognition*, pages 1434–1441. IEEE, 2010. 2
- [17] Silvano Galliani, Katrin Lasinger, and Konrad Schindler. Massively parallel multiview stereopsis by surface normal diffusion. In *Proceedings of the IEEE international conference on computer vision*, pages 873–881, 2015. 2
- [18] Xiaodong Gu, Zhiwen Fan, Siyu Zhu, Zuozhuo Dai, Feitong Tan, and Ping Tan. Cascade cost volume for high-resolution multi-view stereo and stereo matching. In *Proceedings of the IEEE/CVF conference on computer vision and pattern recognition*, pages 2495–2504, 2020. 2
- [19] Guangcong, Zhaoxi Chen, Chen Change Loy, and Ziwei Liu. Sparsenerf: Distilling depth ranking for few-shot novel view synthesis. *IEEE/CVF International Conference on Computer Vision (ICCV)*, 2023. 2, 3
- [20] Ajay Jain, Matthew Tancik, and Pieter Abbeel. Putting nerf on a diet: Semantically consistent few-shot view synthesis. In *ICCV*, pages 5885–5894, 2021. 2, 3
- [21] Mengqi Ji, Juergen Gall, Haitian Zheng, Yebin Liu, and Lu Fang. Surfacerfnet: An end-to-end 3d neural network for multiview stereopsis. In *Proceedings of the IEEE international conference on computer vision*, pages 2307–2315, 2017. 2
- [22] Bernhard Kerbl, Georgios Kopanas, Thomas Leimkühler, and George Drettakis. 3d gaussian splatting for real-time radiance field rendering. *ACM Trans. Graph.*, 42(4):139–1, 2023. 1, 2, 4, 5, 6
- [23] Arno Knapitsch, Jaesik Park, Qian-Yi Zhou, and Vladlen Koltun. Tanks and temples: Benchmarking large-scale scene reconstruction. *ACM Transactions on Graphics (ToG)*, 36(4):1–13, 2017. 2, 5
- [24] Kiriakos N Kutulakos and Steven M Seitz. A theory of shape by space carving. *International journal of computer vision*, 38:199–218, 2000. 2

- [25] Min-Seop Kwak, Jiuhn Song, and Seungryong Kim. Geconerf: Few-shot neural radiance fields via geometric consistency. In *ICML*, pages 18023–18036. PMLR, 2023. 2, 3
- [26] Vincent Leroy, Yohann Cabon, and Jerome Revaud. Grounding image matching in 3d with mast3r, 2024. 1, 2, 3, 6
- [27] Jiahe Li, Jiawei Zhang, Xiao Bai, Jin Zheng, Xin Ning, Jun Zhou, and Lin Gu. Dngaussian: Optimizing sparse-view 3d gaussian radiance fields with global-local depth normalization. In *CVPR*, 2024. 2, 3, 5
- [28] David G Lowe. Object recognition from local scale-invariant features. In *Proceedings of the seventh IEEE international conference on computer vision*, pages 1150–1157. Ieee, 1999. 1, 2
- [29] Ben Mildenhall, Pratul P. Srinivasan, Matthew Tancik, Jonathan T. Barron, Ravi Ramamoorthi, and Ren Ng. Nerf: Representing scenes as neural radiance fields for view synthesis. In *ECCV*, 2020. 1, 2
- [30] Raul Mur-Artal, Jose Maria Martinez Montiel, and Juan D Tardos. Orb-slam: a versatile and accurate monocular slam system. *IEEE transactions on robotics*, 31(5):1147–1163, 2015. 2
- [31] Zak Murez, Tarrence Van As, James Bartolozzi, Ayan Sinha, Vijay Badrinarayanan, and Andrew Rabinovich. Atlas: End-to-end 3d scene reconstruction from posed images. In *Computer Vision—ECCV 2020: 16th European Conference, Glasgow, UK, August 23–28, 2020, Proceedings, Part VII 16*, pages 414–431. Springer, 2020. 2
- [32] Richard A Newcombe, Shahram Izadi, Otmar Hilliges, David Molyneaux, David Kim, Andrew J Davison, Pushmeet Kohi, Jamie Shotton, Steve Hodges, and Andrew Fitzgibbon. Kinectfusion: Real-time dense surface mapping and tracking. In *2011 10th IEEE international symposium on mixed and augmented reality*, pages 127–136. Ieee, 2011. 1
- [33] Michael Niemeyer, Jonathan T. Barron, Ben Mildenhall, Mehdi S. M. Sajjadi, Andreas Geiger, and Noha Radwan. Regnerf: Regularizing neural radiance fields for view synthesis from sparse inputs. In *CVPR*, 2022. 2
- [34] Matthias Nießner, Michael Zollhöfer, Shahram Izadi, and Marc Stamminger. Real-time 3d reconstruction at scale using voxel hashing. *ACM Transactions on Graphics (ToG)*, 32(6):1–11, 2013. 1
- [35] AKM Rabby and Chengcui Zhang. Beyondpixels: A comprehensive review of the evolution of neural radiance fields. *arXiv preprint arXiv:2306.03000*, 2023. 2
- [36] René Ranftl, Katrin Lasinger, David Hafner, Konrad Schindler, and Vladlen Koltun. Towards robust monocular depth estimation: Mixing datasets for zero-shot cross-dataset transfer. *IEEE Transactions on Pattern Analysis and Machine Intelligence*, 44(3), 2022. 4
- [37] Johannes L Schonberger and Jan-Michael Frahm. Structure-from-motion revisited. In *CVPR*, pages 4104–4113, 2016. 1, 3, 5
- [38] Johannes L Schonberger and Jan-Michael Frahm. Structure-from-motion revisited. In *Proceedings of the IEEE conference on computer vision and pattern recognition*, pages 4104–4113, 2016. 2
- [39] Johannes Lutz Schönberger, Enliang Zheng, Marc Pollefeys, and Jan-Michael Frahm. Pixelwise view selection for unstructured multi-view stereo. In *European Conference on Computer Vision (ECCV)*, 2016. 1
- [40] Steven M Seitz and Charles R Dyer. Photorealistic scene reconstruction by voxel coloring. *International journal of computer vision*, 35:151–173, 1999. 2
- [41] Noah Snavely, Steven M. Seitz, and Richard Szeliski. Photo tourism: Exploring photo collections in 3d. In *SIGGRAPH Conference Proceedings*, pages 835–846, New York, NY, USA, 2006. ACM Press. 2
- [42] Jiuhn Song, Seonghoon Park, Honggyu An, Seokju Cho, Min-Seop Kwak, Sungjin Cho, and Seungryong Kim. Därf: Boosting radiance fields from sparse input views with monocular depth adaptation. *Advances in Neural Information Processing Systems*, 36:68458–68470, 2023. 4
- [43] Jiaming Sun, Yiming Xie, Linghao Chen, Xiaowei Zhou, and Hujun Bao. Neuralrecon: Real-time coherent 3d reconstruction from monocular video. In *Proceedings of the IEEE/CVF conference on computer vision and pattern recognition*, pages 15598–15607, 2021. 2
- [44] Mikaela Angelina Uy, Ricardo Martin-Brualla, Leonidas Guibas, and Ke Li. Scade: Nerfs from space carving with ambiguity-aware depth estimates. In *Proceedings of the IEEE/CVF Conference on Computer Vision and Pattern Recognition*, pages 16518–16527, 2023. 4
- [45] Ashish Vaswani, Noam Shazeer, Niki Parmar, Jakob Uszkoreit, Llion Jones, Aidan N Gomez, Łukasz Kaiser, and Illia Polosukhin. Attention is all you need. In *Advances in Neural Information Processing Systems*. Curran Associates, Inc., 2017. 3
- [46] Fangjinhua Wang, Silvano Galliani, Christoph Vogel, Pablo Speciale, and Marc Pollefeys. Patchmatchnet: Learned multi-view patchmatch stereo. In *Proceedings of the IEEE/CVF conference on computer vision and pattern recognition*, pages 14194–14203, 2021. 2
- [47] Fangjinhua Wang, Qingtian Zhu, Di Chang, Quankai Gao, Junlin Han, Tong Zhang, Richard Hartley, and Marc Pollefeys. Learning-based multi-view stereo: A survey. *arXiv preprint arXiv:2408.15235*, 2024. 2
- [48] Kaixuan Wang and Shaojie Shen. Mvdepthnet: Real-time multiview depth estimation neural network. In *2018 International conference on 3d vision (3DV)*, pages 248–257. IEEE, 2018. 2
- [49] Shuzhe Wang, Vincent Leroy, Yohann Cabon, Boris Chidlovskii, and Jerome Revaud. Dust3r: Geometric 3d vision made easy. In *CVPR*, 2024. 1, 2, 3
- [50] Zhou Wang, Alan C Bovik, Hamid R Sheikh, and Eero P Simoncelli. Image quality assessment: from error visibility to structural similarity. *IEEE transactions on image processing*, 13(4):600–612, 2004. 5
- [51] Haolin Xiong, Sairisheek Muttukuru, Rishi Upadhyay, Pradyumna Chari, and Achuta Kadambi. Sparsegs: Real-time 360° sparse view synthesis using gaussian splatting. *Arxiv*, 2023. 2, 3
- [52] Chen Yang, Sikuang Li, Jiemin Fang, Ruofan Liang, Lingxi Xie, Xiaopeng Zhang, Wei Shen, and Qi Tian. Gaussianob-

- ject: High-quality 3d object reconstruction from four views with gaussian splatting. In *ACM TOG*, 2024. 3
- [53] Jiawei Yang, Marco Pavone, and Yue Wang. Freenerf: Improving few-shot neural rendering with free frequency regularization. In *CVPR*, 2023. 2, 3
- [54] Lihe Yang, Bingyi Kang, Zilong Huang, Zhen Zhao, Xiaogang Xu, Jiashi Feng, and Hengshuang Zhao. Depth anything v2. *arXiv preprint arXiv:2406.09414*, 2024. 5
- [55] Ruigang Yang and Marc Pollefeys. Multi-resolution real-time stereo on commodity graphics hardware. In *2003 IEEE Computer Society Conference on Computer Vision and Pattern Recognition, 2003. Proceedings.*, pages I–I. IEEE, 2003. 2
- [56] Yao Yao, Zixin Luo, Shiwei Li, Tian Fang, and Long Quan. Mvsnnet: Depth inference for unstructured multi-view stereo. In *Proceedings of the European conference on computer vision (ECCV)*, pages 767–783, 2018. 2
- [57] Vickie Ye, Ruilong Li, Justin Kerr, Matias Turkulainen, Brent Yi, Zhuoyang Pan, Otto Seiskari, Jianbo Ye, Jeffrey Hu, Matthew Tancik, and Angjoo Kanazawa. gsplat: An open-source library for Gaussian splatting. *arXiv preprint arXiv:2409.06765*, 2024. 5
- [58] Xianggang Yu, Mutian Xu, Yidan Zhang, Haolin Liu, Chongjie Ye, Yushuang Wu, Zizheng Yan, Chenming Zhu, Zhangyang Xiong, Tianyou Liang, et al. Mvimngnet: A large-scale dataset of multi-view images. In *Proceedings of the IEEE/CVF conference on computer vision and pattern recognition*, pages 9150–9161, 2023. 2, 5, 6
- [59] Christopher Zach, Thomas Pock, and Horst Bischof. A globally optimal algorithm for robust tv-l1 range image integration. In *2007 IEEE 11th International Conference on Computer Vision*, pages 1–8. IEEE, 2007. 2
- [60] Richard Zhang, Phillip Isola, Alexei A Efros, Eli Shechtman, and Oliver Wang. The unreasonable effectiveness of deep features as a perceptual metric. In *Proceedings of the IEEE conference on computer vision and pattern recognition*, pages 586–595, 2018. 5
- [61] Enliang Zheng, Enrique Dunn, Vladimir Jovic, and Jan-Michael Frahm. Patchmatch based joint view selection and depthmap estimation. In *Proceedings of the IEEE conference on computer vision and pattern recognition*, pages 1510–1517, 2014. 2
- [62] Zehao Zhu, Zhiwen Fan, Yifan Jiang, and Zhangyang Wang. Fsgs: Real-time few-shot view synthesis using gaussian splatting. In *ECCV*, 2024. 2, 3